



# Compositional Effects and Optical Properties of P<sub>2</sub>O<sub>5</sub> Doped Magnesium Silicate Mesoporous Thin Films

Amany M. El Nahrawy<sup>1</sup> · Ali B. Abou Hammad<sup>1</sup> · A. M. Mansour<sup>1</sup>

Received: 3 June 2020 / Accepted: 23 October 2020 / Published online: 11 November 2020  
© King Fahd University of Petroleum & Minerals 2020

## Abstract

Mesoporous P<sub>2</sub>O<sub>5</sub> doped magnesium silicate (MS-P) thin films were prepared using the activated sol–gel method and calcinated at different temperatures (200, 300, and 400 °C). The effect of both P<sub>2</sub>O<sub>5</sub> content, and the calcinating temperature on the thin films structure, morphology, FTIR, and UV–Vis optical properties, was examined. The structural results demonstrate that the changing of the P<sub>2</sub>O<sub>5</sub> content ratio and the temperature of preparation have significant effects on crystallization and the internal structure. All films were found to have a relative value of transmittance that reaches or exceeds about 90% in the visible range. The optical band gap shows a blue shift with increasing of the P<sub>2</sub>O<sub>5</sub> content as well as with calcinating temperature increase. The refractive index is nearly constant and uniform in the overall visible zone for all samples. The optical conductivity shows nearly relative values and similar behaviors in all P<sub>2</sub>O<sub>5</sub> contents at all calcinating temperatures, where it is constant at low energies and increases at higher incident photon energies.

**Keywords** Magnesium silicate · Phosphate · Sol–gel · Mesoporous · Thin films · Optical

## 1 Introduction

Due to their exact interesting photoluminescence, optical, biomedical and electrical properties in combination with their non-toxicity, non-hygroscopic nature, and lower cost, optical materials containing P<sub>2</sub>O<sub>5</sub> have been well regarded as low-temperature glasses of the scientific and technological fields [1–3]. Because of their interest in laser, optoelectronics, and fiber optics applications, developments in the physical properties of the silicate network have been studied widely [4, 5]. It is well-known that the phosphate glasses exhibited unique properties such as low optical basicity, softening temperature, high thermal expansion coefficients, low refractive index, high electrical conductivity, low glass transition, and High transparency range (185 nm–3 μm) have produced various optical applications including fast ion-conducting materials, solid-state electrolytes, high-performance lasers, biocompatible engineering materials [6, 7]. Moreover, the problems connected with Phosphate glasses may limit their

application in future industrial and electronic devices. Otherwise, the chemical durability and structure of the phosphate system could be developed by doping or adding another glass former and various modifiers similar to Al<sub>2</sub>O<sub>3</sub>, SiO<sub>2</sub>, Co<sub>2</sub>O<sub>3</sub>, ZnO, MgO, and rare earth ions [8–10].

The optical silicate/phosphate glasses are of particular interest as hosts for rare earth ions where it merges the favorable optical properties of silicate glasses and the higher chemical and thermal stability of the phosphate glass. Also, the combinations of silicate polyhedral with P<sub>2</sub>O<sub>5</sub> anions lead to improvements of their chemical stability, sensitivity to loading higher active ions, large exciting binding energy, and greater transparency in the UV regions [11–13].

The replacement of some Si–O by P–O in magnesium silicate matrix improves the solubility, chemical durability, calcination temperature, and resistance to attack by (–OH), owing to the advantageous properties produced from the introduction of P<sub>2</sub>O<sub>5</sub> in the tetrahedral silicate network [14–16]. In the silicate system, MgO and P<sub>2</sub>O<sub>5</sub> modifiers are deliberated to be occupying the positions enclosed by the (NBO) non-bridging oxygen belonging to SiO<sub>4</sub>-tetrahedra network and phosphate, which strengthening and opening the silicate network [17].

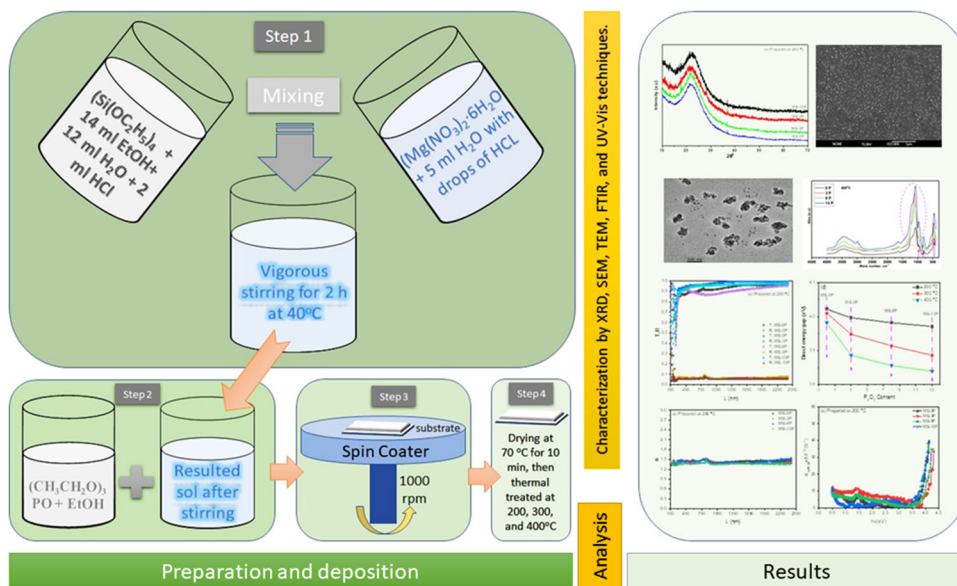
Topical progress in the formation of nano silicate films established on the forward sol–gel preparation has signif-

✉ A. M. Mansour  
amamansour@gmail.com

<sup>1</sup> Solid-State Physics Department, Physics Research Division, National Research Centre, 33 El-Bohouth St., Dokki, Giza 12622, Egypt



**Fig. 1** Schematic diagram of preparation steps, characterization techniques, and obtained results



icantly supported the progress of highly transparent nano silicate films. Silicate particles with altered particle morphologies and sizes have been formed using the sol–gel practice through controlling different parameters like the alkoxide concentration, ratio of alkoxide/solvent, the quantity of water, pH, solvent type, and thermal treatment [5, 18].

This study aims to tailor the physical properties of mesoporous magnesium silicate/phosphate films prepared using sol–gel/spinning coating as an attractive high transparent film to detailed demands in the optical application domain involves an understanding of their structural strategies.

Because of its polyprotic property, phosphoric acid is used as a precipitating agent, which can control the hydrolysis reaction and particle formation. Additionally, this acid is commonly used in the food, medicine, and dentistry industries. A systematic study of parameters affects the formation of silica particles has been carried out. The physical and chemical properties of silica have been investigated to determine its possibility as a low-cost biomaterial filler for applications in dental restoration.

## 2 Experimental

### 2.1 Materials and Preparation

The chemicals that used in this study were magnesium nitrate ( $\text{Mg}(\text{NO}_3)_2 \cdot 6\text{H}_2\text{O}$ , Aldrich), tetraethylorthosilicate ( $\text{Si}(\text{OC}_2\text{H}_5)_4$ , TEOS, Fluka), triethyl phosphate ( $(\text{CH}_3\text{CH}_2\text{O})_3\text{PO}$ , TEP, Aldrich), absolute ethanol (EtOH, commercial-grade), and hydrochloric acid (HCl, commercial grade).

The formed (0, 3, 8, and 13 wt%)  $\text{P}_2\text{O}_5$ /magnesium silicate (MS-P) thin films were produced through four steps preparation process as schematically presented in Fig. 1.

The first step was the preparation of two solutions. The first one was a solution of magnesium nitrate  $\text{Mg}(\text{NO}_3)_2 \cdot 6\text{H}_2\text{O}$  in a mixture of 9 ml of tetraethylorthosilicate ( $\text{Si}(\text{OC}_2\text{H}_5)_4$ , 14 ml of absolute ethanol (EtOH), 12 ml deionized water, and 2 ml of HCl. The second one was a solution of magnesium acetate ( $\text{Mg}(\text{NO}_3)_2 \cdot 6\text{H}_2\text{O}$  in 5 ml  $\text{H}_2\text{O}$  with a drop of HCl. The two pre-prepared solutions were then mixed under vigorous stirring for 2 h at 40 °C. The second step was adding a different concentration (0, 3, 8, and 13 wt%) of a  $\text{P}_2\text{O}_5$ /(TEP and EtOH mixture) to the mixture resulting from step one. Where the  $\text{P}_2\text{O}_5$  loaded within the sol of magnesium silicate matrix was provided by the same method. A  $\text{P}_2\text{O}_5$  solution was prepared using TEP/EtOH under magnetic stirring for 15 min before introduced to the MS sol then stirred for 1 h and becomes ready for depositing as wet MS-P thin films. In which the TEP/EtOH precursors could facily undergo catalyzed the hydrolysis and condensation reactions within MS sol in the formation of a sol of MS-P metal oxide particles at the nanoscale.

This method is comparable to the procedures that have been working via other authors [19, 20]. Now, we reach the third step where the prepared sols are ready to be deposited on precleaned glass substrates using the spin-coating technique at 1000 rpm for 30 s. the resulted thin films are then dried at 70 °C for 10 min before thermally calcinated at 200 °C, 300 °C, and 400 °C, which was the fourth and the last step of the preparation process.

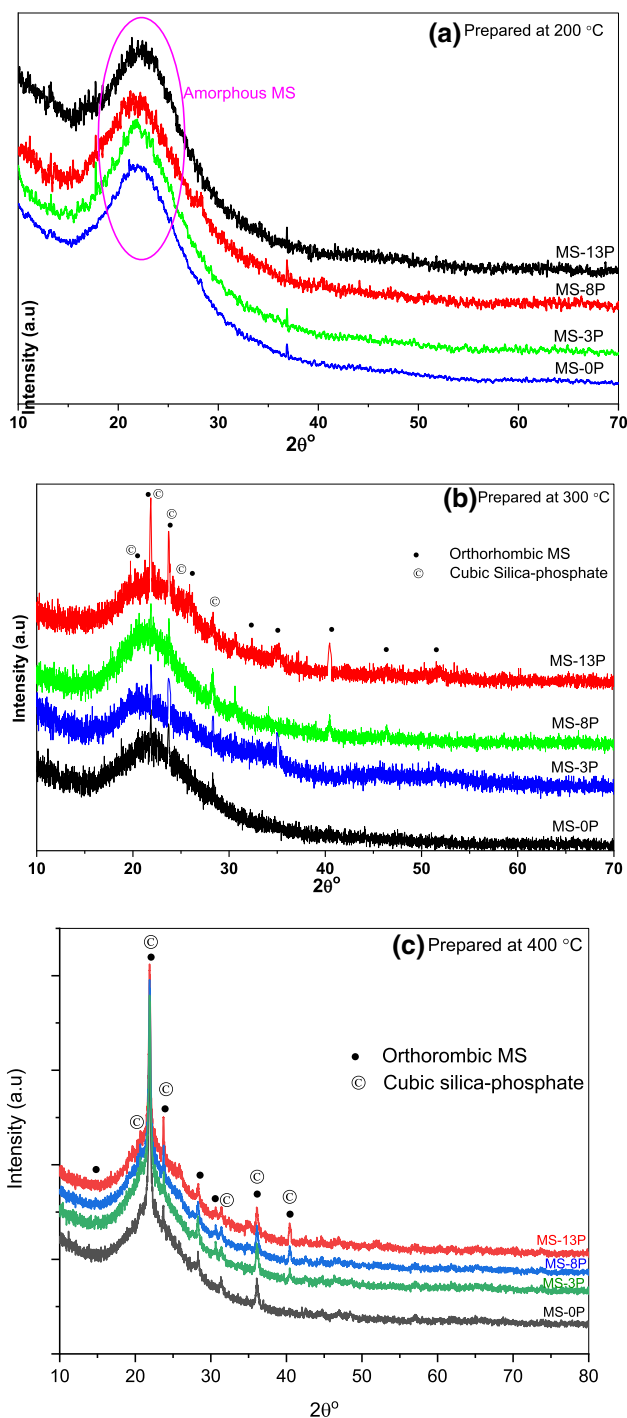


**Fig. 2** XRD spectra for MS doped with (0, 3, 8, and 13) P<sub>2</sub>O<sub>5</sub> calcinated at **a** 200 °C, **b** 300 °C and **c** 400 °C

## 2.2 Characterization

In the characterization process, the prepared thin films were subjected to structural, morphological, and optical analysis as schematically presented in Fig. 1. The employed approaches are described in the following lines.

X-ray diffraction (Bruker: D8-X-ray Diffractometer, Germany fortified by CuK $\alpha$  ( $\lambda = 1.54$  nm)) was employed in the range  $2\theta$  ( $10^\circ$ – $80^\circ$ ) at 40 mV and 30 mA to explore the structural properties of the prepared films. The presence of miscellaneous phases has been recognized by comparing the experimental data by the JCPDS data files in Pcpdftwin-software. The crystal size of MS-P films is extracted from the XRD results through the use of Scherrer’s formula [21]:

$$D = 0.94 \frac{\lambda}{\beta \cos \theta} \tag{1}$$

where  $D$  gives the crystal size,  $\lambda$  is the wavelength of X-Ray (0.179 nm),  $\theta$  is the half diffraction angle of the peak, and  $\beta$  the true half peak width.

The surface morphology of the films was observed and photographed by scanning electron microscopy (SEM) (Joel—JSM:6480 LV, Japan).

The particle nano-size of film samples was checked by the transmission electron microscope (TEM) (JEM-2100, Jeol, Japan). The prepared films were etched in a solution of (HF/H<sub>2</sub>O) and then takes into the carbon grid to be tested by TEM. The prepared films were etched in a solution of (HF/H<sub>2</sub>O) and then takes into the carbon grid to be tested by TEM.

The Fourier transform infrared spectra (FTIRs) for each film were recorded between 400 to 4000  $\text{cm}^{-1}$  for 32 scans by a Thermo Nicolet-380 spectrometer, with a resolution of 0.5  $\text{cm}^{-1}$ .

The optical spectra were recorded by an optical spectrophotometer (Jasco, V-570) spectrophotometer in the range 0.2–2.5  $\mu\text{m}$ .

## 3 Results and Discussions

### 3.1 Structural Analysis

The X-ray diffraction spectra for (0–13 mol%) P<sub>2</sub>O<sub>5</sub>-magneso-silicate transparent films using advanced sol–gel process and calcinated at 200, 300, and 400 °C are shown in Fig. 2.

The appeared broadband among  $2\theta = 17^\circ$ – $28^\circ$  in all XRD pattern is due to the identified amorphous order of the magnesium silica matrix [22]. The amorphous nature of the prepared films has been analyzed from its evaluated XRD-presented in Fig. 2a. The decrease in crystallinity correlated with the increase in the disheveled range ordered in the three-dimensional magnesium silicate networks. The appearance of some weak peaks which indicates that P<sub>2</sub>O<sub>5</sub> was incorporated into the MS matrix as a definitive product. A higher crystalline pattern with an obvious crystalline phase was exposed to the mesoporous films calcinated at 300 °C,

**Fig. 3** SEM images of MS doped with  $P_2O_5$  nanoparticles **a** 0, **b** 3, **c** 13 mol%, and **d** EDX of MS-3P calcinated at 400 °C

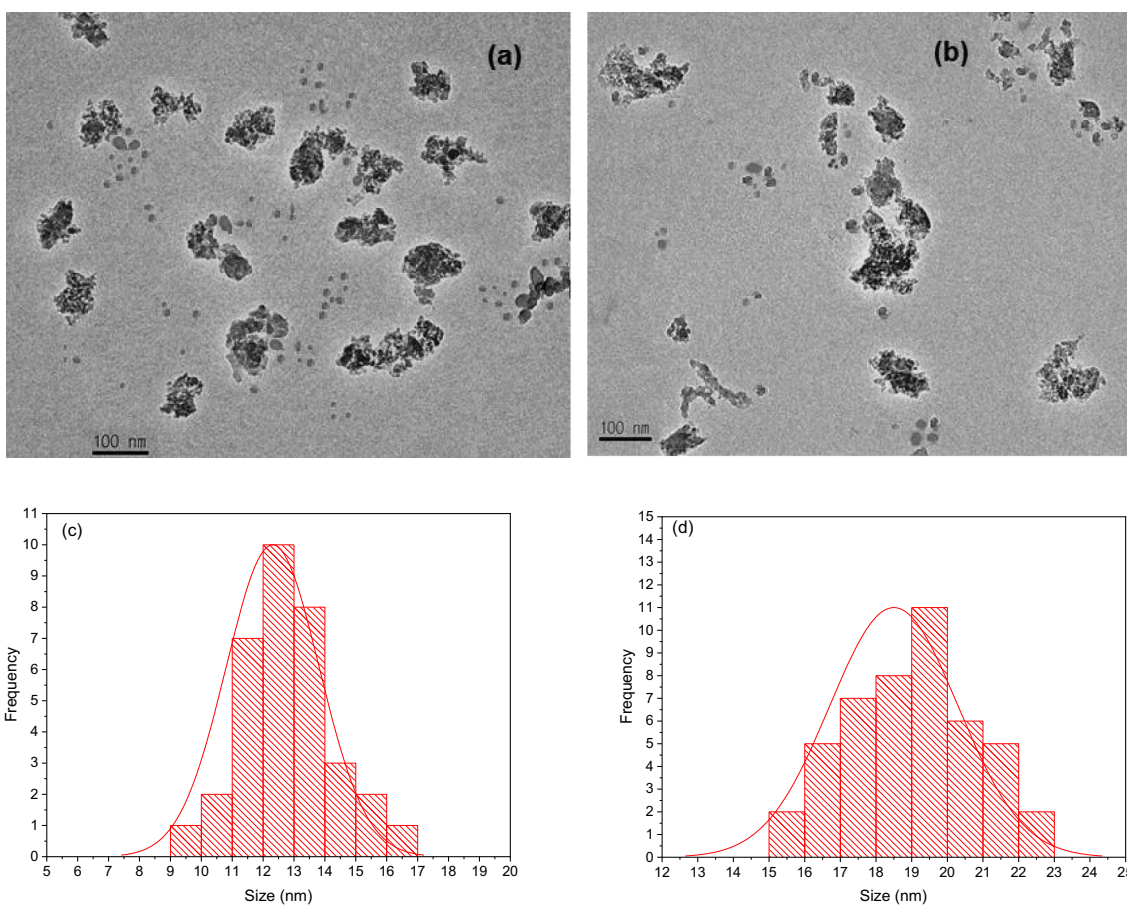
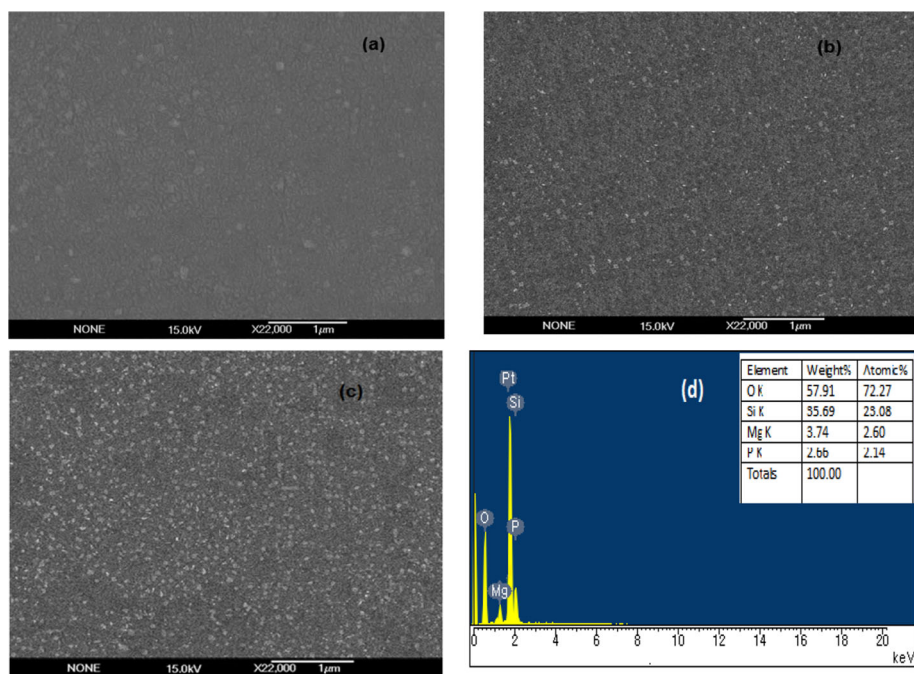


**Fig. 4** TEM image of MS doped with  $P_2O_5$  nanoparticles **a** 0 and **b** 13 mol% calcinated at 400 °C and their corresponding particle distributions in **c** and **d**, respectively,

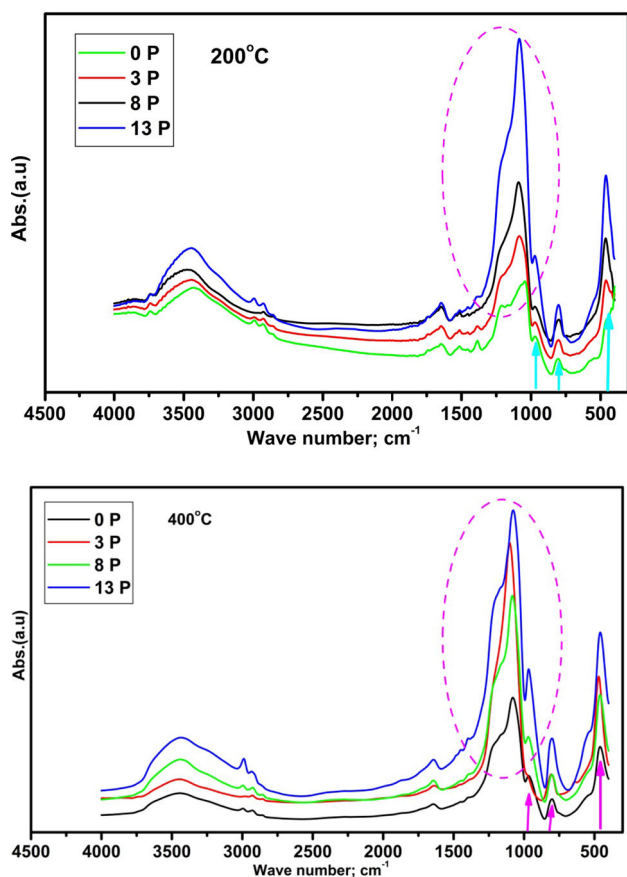


**Fig. 5** FTIR spectra for MS doped with (0, 3, 8, and 13) P<sub>2</sub>O<sub>5</sub> calcinated at 200 °C and 400 °C

Fig. 2b. The obvious board and weak peaks correspond to the orthorhombic magnesium silicate crystalline phase (JCPDS: 80-1764) and cubic silica-phosphate (JCPDS: 22-1274). The characteristic diffraction peaks of magnesium silicate doped with P<sub>2</sub>O<sub>5</sub> were grown and it appears to be the only demonstrated phase by XRD. For P<sub>2</sub>O<sub>5</sub>, no single phase has any perceptible XRD peaks, further; the illustrative peak at nearly 21.86° regularly becomes more intense and sharper as the film's calcination temperature increases at 400 °C, Fig. 2c. Confirming that magnesium silicate–phosphate matrix were consists of alternately assemble Si–O (silicon–oxygen tetrahedral), Si–O–P sites, and Mg–O (magnesium–oxygen) sites with higher chains [17]. The obtained result is in agreement with that described by the literature [20]. The deduced crystal-size for the MS and MS-P calcinated at 400 °C are 14 nm and 18 nm, respectively.

### 3.2 Morphological Analysis

Figure 3 shows SEM-images of the magnesium silicate doped with (0, 3, 13 mol%) P<sub>2</sub>O<sub>5</sub> mesoporous films calcinated at 400 °C.

SEM analysis revealed the existence of a higher crystalline degree for P<sub>2</sub>O<sub>5</sub>-MS nanoparticles which is in line with the obtained from the XRD-result. The SEM-images expose a smooth morphology with low accumulation. Figure 3b, c showed that the morphologies of P<sub>2</sub>O<sub>5</sub>-magnesium silicate nanoparticles were more spherical particles and more widely distributed as the P<sub>2</sub>O<sub>5</sub> content increased, which promote the growth in the formed films. At higher P<sub>2</sub>O<sub>5</sub> content, the hard cross-linkage film is formed in the magnesium silicate matrix, leading to hard agglomerated nanoparticles during the thermal calcinated.

TEM images of magnesium silicate mesoporous transparent films modified with the introduction of P<sub>2</sub>O<sub>5</sub> (0 and 13 wt%) and calcinated at 400 °C are shown in Fig. 4.

Without P<sub>2</sub>O<sub>5</sub>, the MS nanoparticle film was irregular in shape, and some spherical nanoparticles (Fig. 4a). With introducing (13 mol%) of P<sub>2</sub>O<sub>5</sub>, a spherical shape with some dispersed nanoparticles is detected as in Fig. 4b. This might be due to the higher cross-linkage of P<sub>2</sub>O<sub>5</sub> in the MS matrix that accelerates the interpenetration through the silicate-based precursor. Figure 4c, d for the particle's distribution of MS and MS-13 mol% P shows the generated changes in the formed samples. The average particle sizes for the MS and MS-P film samples were 13 nm and 19 nm, respectively. Figure 2d confirms the surface composition of the MS-3P film given by the EDX-analysis.

### 3.3 FTIR Study

The FTIR absorption spectra of the magnesium silicate doped with (0, 3, 13 mol%) P<sub>2</sub>O<sub>5</sub> mesoporous films calcinated at 200 °C and 400 °C are presented in Fig. 5.

The main characteristic position peaks of magnesium silicate in comparison with the doped P<sub>2</sub>O<sub>5</sub> films are obvious in IR spectra. The characteristic frequencies of the bands in the main region (400–1100 cm<sup>-1</sup>) for magnesium silicate-based and doped depend on the lattice vibrations including tetrahedral SiO<sub>2</sub> and SiO<sub>2</sub>-P<sub>2</sub>O<sub>5</sub> metal ions. The strong bands for MS and MS-P were observed at 1077, 967, 809, and 442 cm<sup>-1</sup> in the main region for the FTIR spectrum of undoped MS film in comparison with the doped P<sub>2</sub>O<sub>5</sub> films all bands nearly shifted to higher wavenumber. Herein the introduction of P<sub>2</sub>O<sub>5</sub> in MS matrix promoting the formation of chemical bonds (–Si–O–S, Si–O–P, Mg–O–Si–O–OH, –Si–OH) and non-bridging oxygen (Si–O–NBO) groups that construct more clustering particles during the sol aging process and film densification [23].

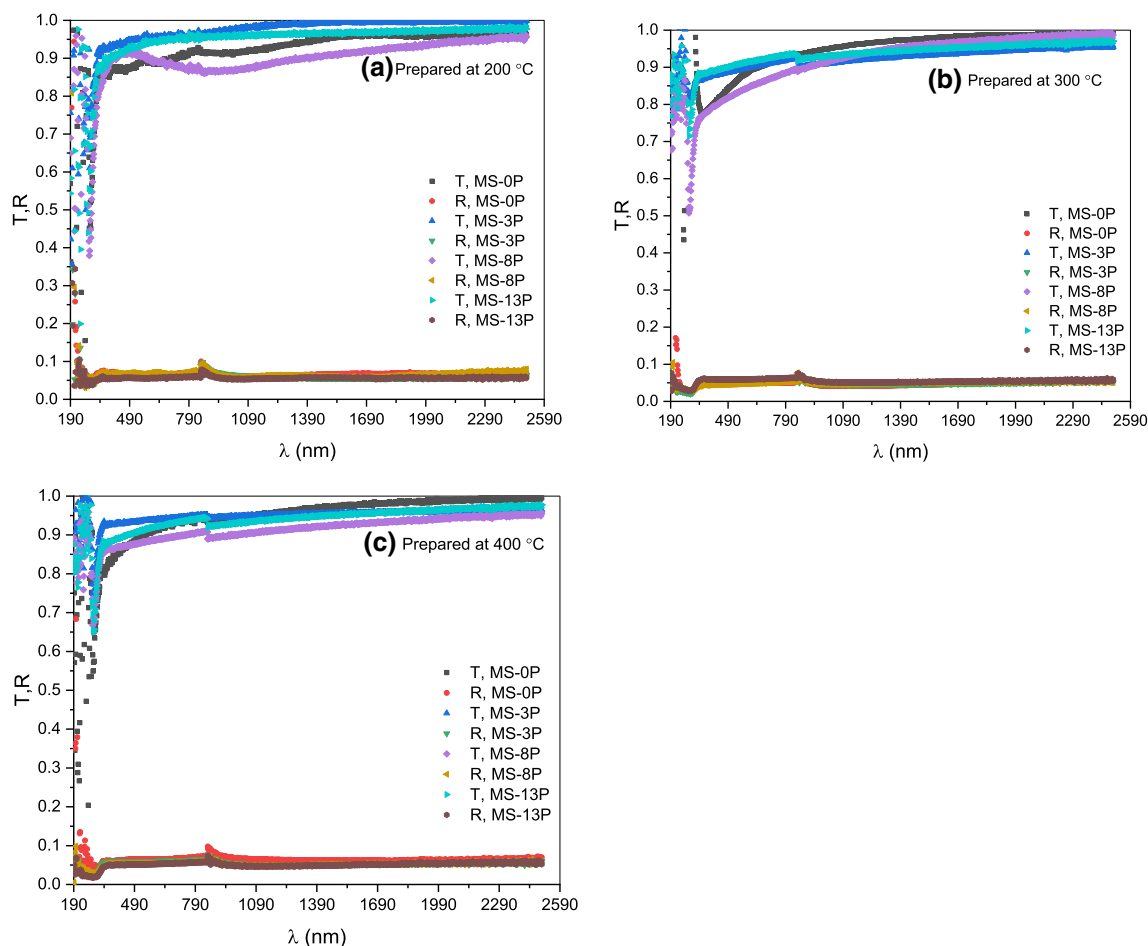


**Fig. 6** The optical transmittance and reflectance spectra of the prepared thin films calcinated at different temperatures in the range 200–2500 nm wavelengths

The doped nanoporous films appear changing in the band's intensities and brooding at 1077, 809, and 442  $\text{cm}^{-1}$  assigned to the internal arrangement in Si–O–Si and Si–O–Mg bands with introducing P–O vibration modes of  $\text{PO}_4$  [24]. This is an important step of the silicate sol–gel process since the concentration of (Si–O–NBO) groups regulator the rate of silica dissolution by forming silanol-groups at the MS film surface [3, 5]. This reveals that the sol–gel MS-network is chemically sensitive to the changes in their compositions may because  $\text{P}_2\text{O}_5$  is completely cross-linkage in the silicate network [25].

The change of absorption band at 1077, 442 and the shoulder 1211  $\text{cm}^{-1}$  for MS and MS-P with increasing the calcination temperature is confirmed good formation polycrystalline films. The shoulder at 1211  $\text{cm}^{-1}$  shows the existence of asymmetric stretching of Si–O–Si, Si–O–Mg, and  $(\text{PO}_3)_2$ -groups in magnesium silicate matrix [26].

The bands at 1077, 971, 805, and 442  $\text{cm}^{-1}$  characterized the asymmetric stretching, symmetric, and the bending vibrations of Si–O–Si, Si–O–Mg, and P–O–P, in magnesium silicate network [27–29]. The effect of increasing calcination

temperature on the tetrahedral metal–oxygen bonds in the prepared nanoporous films can be interpreted via the elimination of (–OH) group and the formation of additional covalent bonding of metal ions; hence, the sharpness of the absorption bands for the films calcinated at 400 °C was larger than the films at 200 °C. The three absorption bands, two ones at 3463 and 3742  $\text{cm}^{-1}$ , which was ascribed to the stretching of hydroxyl groups (–OH s:) and third at  $\sim 1651 \text{ cm}^{-1}$ , which is attributed to physisorbed (bending of  $\text{H}_2\text{O}$ ), and these bands shifted to lower wavenumber with higher calcination temperature as presented in the Fig. 5 [30].

### 3.4 UV–Vis Optical Analysis

When light passes through a semiconductor layer material, a portion is reflected, a portion is transmitted, and the others are absorbed. Photons absorption motives the passage of the electrons from the valence to the conduction band. The optical band gap is looked as the least energy required for an electron excitation from the lower to higher energy

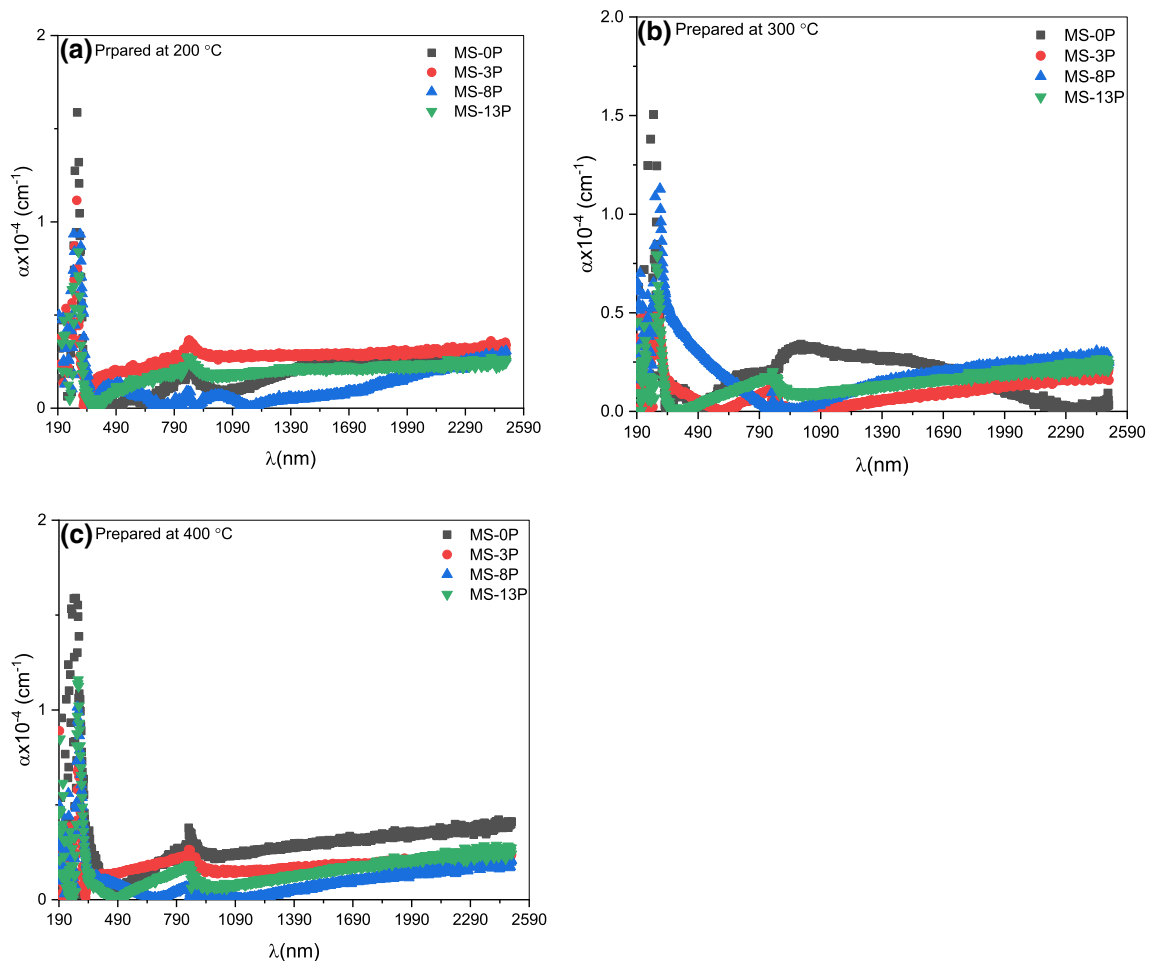


**Fig. 7** The absorption coefficient of the prepared thin films calcinated at different temperatures in the range 200–2500 nm wavelengths

band [31–33]. Intrinsic absorption happens when the photon energy lies in the range of the material energy band-gap. The possibility of absorption is identified by its absorption coefficient ( $\alpha$ ) which is estimated by utilizing Beer–Lambert’s formulation [34–37],

$$\alpha = 2.303A/d \tag{2}$$

where  $A$  and  $d$  represent the absorbance and the film thickness.

The incident photon energy absorption lead to direct or indirect optical transitions which are calculated through Tauc’s method [38, 39],

$$\alpha = \frac{A}{hv} (hv - E_g)^n \tag{3}$$

where  $hv$ ,  $A$ ,  $E_g$ , and  $n$  representing the wave energy, the absorption edge width parameter, the optical band gap, and a constant, respectively.  $n = 1/2$  for allowed direct type, and  $n = 2$  for allowed indirect type [40]. The values of the direct

band-gap energy were estimated by plotting  $(\alpha hv)^2$  versus  $hv$  and by linear extrapolation of  $(\alpha hv)^2$  on  $hv$  axis.

In the present work, the transmittance and absorption spectra of P doped  $MgSiO_3$  (0, 3, 8, and 13 wt%) thin films calcinated at different temperatures (200, 300, and 400 °C) are recorded by a Jasco V-570 spectrophotometer in the wavelength range 0.2–2.0  $\mu m$ .

The optical transmittance and reflectance spectra of the prepared thin films between 200–2500 nm wavelengths are shown in Fig. 6 (a, b, and c for the preparation temperature 200, 300, and 400 °C, respectively). All films have a relative value of transmittance that reaches or exceeds about 90% in the visible range. It was noted that the surface scattering and the grain boundary scattering are the main factors impacting the film transmittance.

The absorption coefficient  $\alpha$  in Eq. (2) is composed of two components ( $\alpha = \alpha_\alpha + \alpha_s$ ), where  $\alpha_\alpha$  is the material absorption coefficient, and  $\alpha_s$  is the scattering coefficient that is dependent upon surface roughness. The absorption coefficient of a sample could be virtually zero, but the scattering coefficient is comparatively considerable. For homogeneous

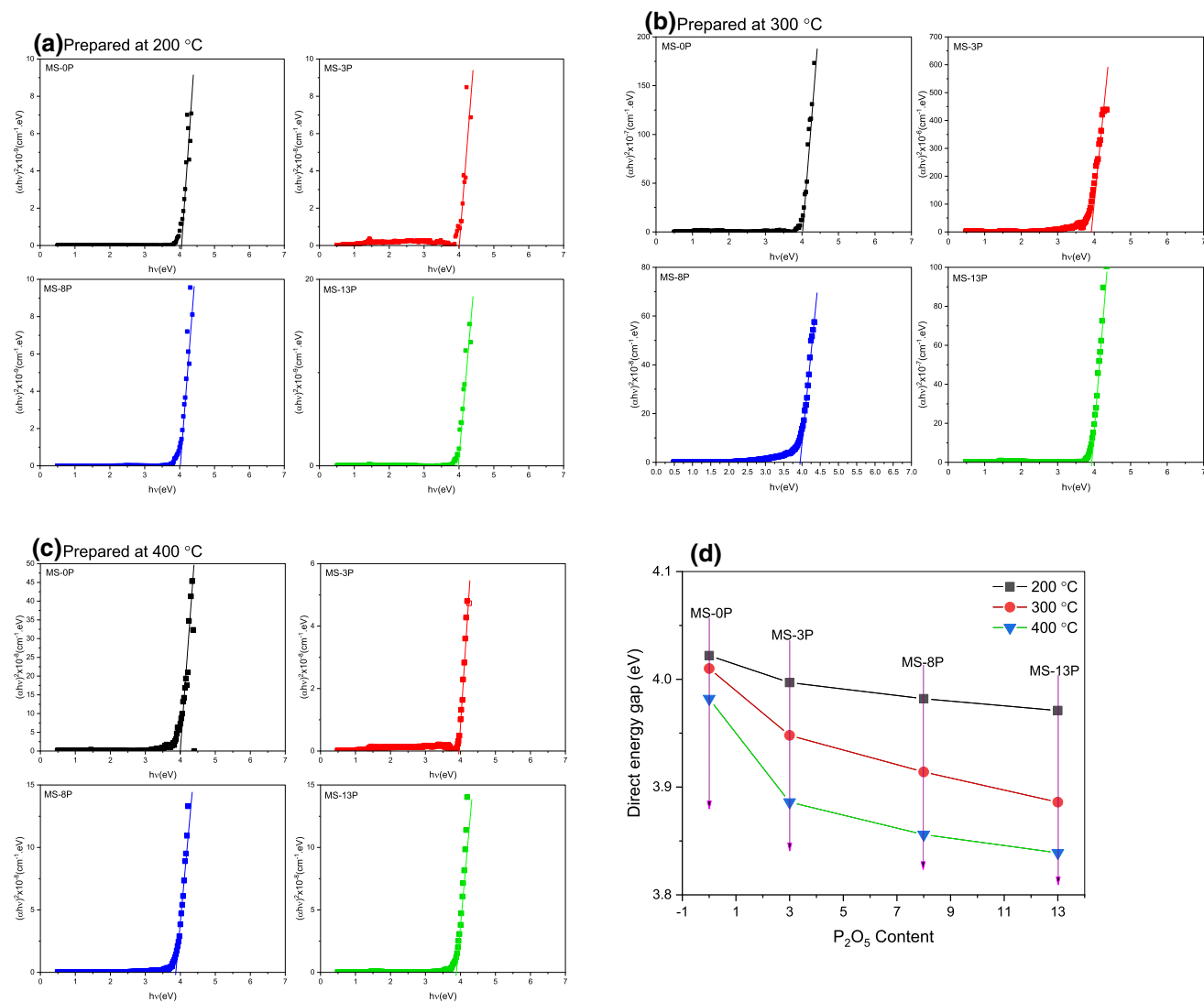


**Fig. 8** The estimation of direct  $E_g$  from the relation between  $h\nu$  and  $(\alpha h\nu)^2$  for thin films calculated at different temperatures (200, 300, and 400 °C)

and isotropic medium, the absorbance,  $A$ , can be acquired instantly via the obtained transmittance, ( $T = I/I_0$ ), by:

$$A = \log\left(\frac{1}{T}\right) \quad (4)$$

For rough materials, reflection, and transmission are significantly affected by the surface roughness degree [41]. Consequently, each of diffusely reflected and transmitted light exist at this point [41].

To comprehend the way the optical benefits were influenced by the surface roughness, Kanyathare et al. [41] studied the impact of roughness on the optical benefits of some polymer sheets. They observed that the sample with the smallest surface roughness offers the greatest transmittance while the samples with the largest surface roughness provide the smallest transmittance. Certainly, raising the degree of sur-

face roughness accelerates the light scattering that lowers the transmittance [41].

In this situation, it will be easy to compute the surface roughness the measured transmittance by employing the Gaussian roughness distribution function offered by Niskanen et al. [42],

$$T = T_0 \exp\left(-\left(2\pi R_{\text{opt}} n \lambda^{-1} \cos \theta\right)^2\right) \quad (5)$$

where  $T_0$  is the transmittance of smooth surface,  $R_{\text{opt}}$  is the optical roughness,  $\theta$  is an angle between a light ray and the optical axis of the specimen. The model of Niskanen [42] matches best for conditions that the average roughness is smaller than the probe light wavelength.

The surface of the prepared films is relatively smooth with a regular grain boundary (as obtained by SEM and TEM images) resulting in weak scattering and therefore inducing



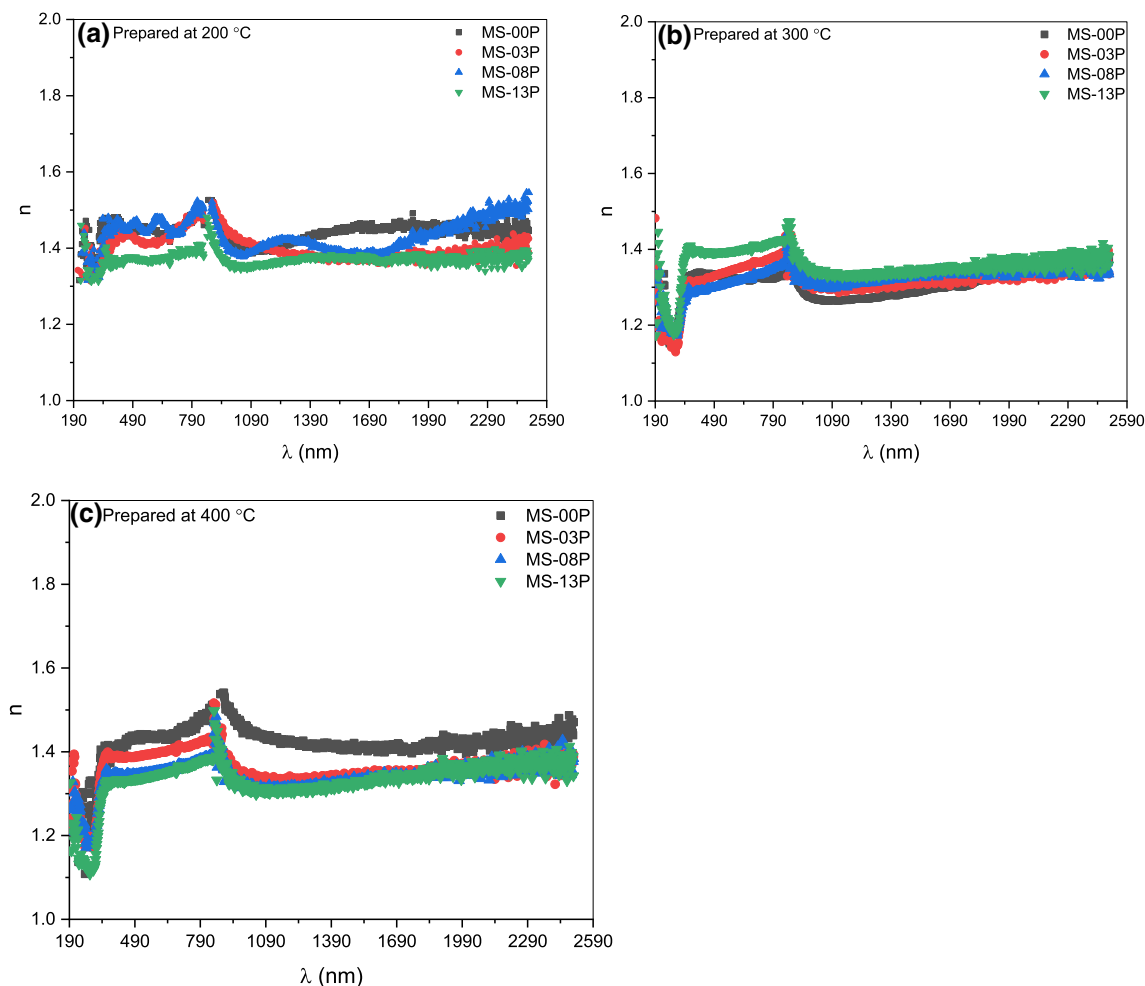


**Fig. 9** The refractive index  $n$  of the prepared thin films with different  $P_2O_5$  concentrations and at different calcination temperatures

a good transmittance within the visible part of the spectra [43]. The reflectance of all prepared films at all preparation temperatures is in the range of 5% or less and did not show any change with wavelength increase.

From the UV–visible absorption spectra, Fig. 7, it can be seen that existing of an absorption peak at about 273 nm for all films calcinated at different temperatures. This absorption peak has resulted from the charge carrier’s excitation and transition from valance band to conduction band [21, 32].

The optical band gap  $E_g$  was estimated using the Tauc procedure mentioned in Eq. (3). The investigated films showed a direct gap transition where its values were predicted by just an extrapolate of the straight section of the resulted curve to  $(\alpha h\nu)^2 = 0$  [14, 44] as shown in Fig. 8.

It could be viewed that the optical band gap exhibits a blue shift with increasing the  $P_2O_5$  content and with preparation temperature increase.

The replacement of some Si–O by P–O in magnesium silicate matrix improves the solubility, chemical durability, calcination temperature, and resistance to attack by (–OH),

owing to the advantageous properties produced from the introduction of  $P_2O_5$  in the tetrahedral silicate network [14–16]. In the silicate system, MgO and  $P_2O_5$  modifiers are deliberated to be occupying the positions enclosed by the (NBO) non-bridging oxygen belonging to the  $SiO_4$ -tetrahedra network and phosphate, which strengthening and opening the silicate network [17], that lead to a better crystallinity and the decreasing defects of the thin films (as observed by XRD and SEM) which influenced the band-gap energy [45, 46].

The refractive index is a reflection of the optical quality of the investigated thin films. At the same time, it also reflects the degree of the crystalline quality of the thin films. From the spectral transmittance and the reflectance ( $R$ ), the refractive index ( $n$ ) is computed using [47–49].

$$n = \frac{1 + R}{1 - R} + \sqrt{\frac{4R}{(1 - R)^2} - k^2} \tag{5}$$

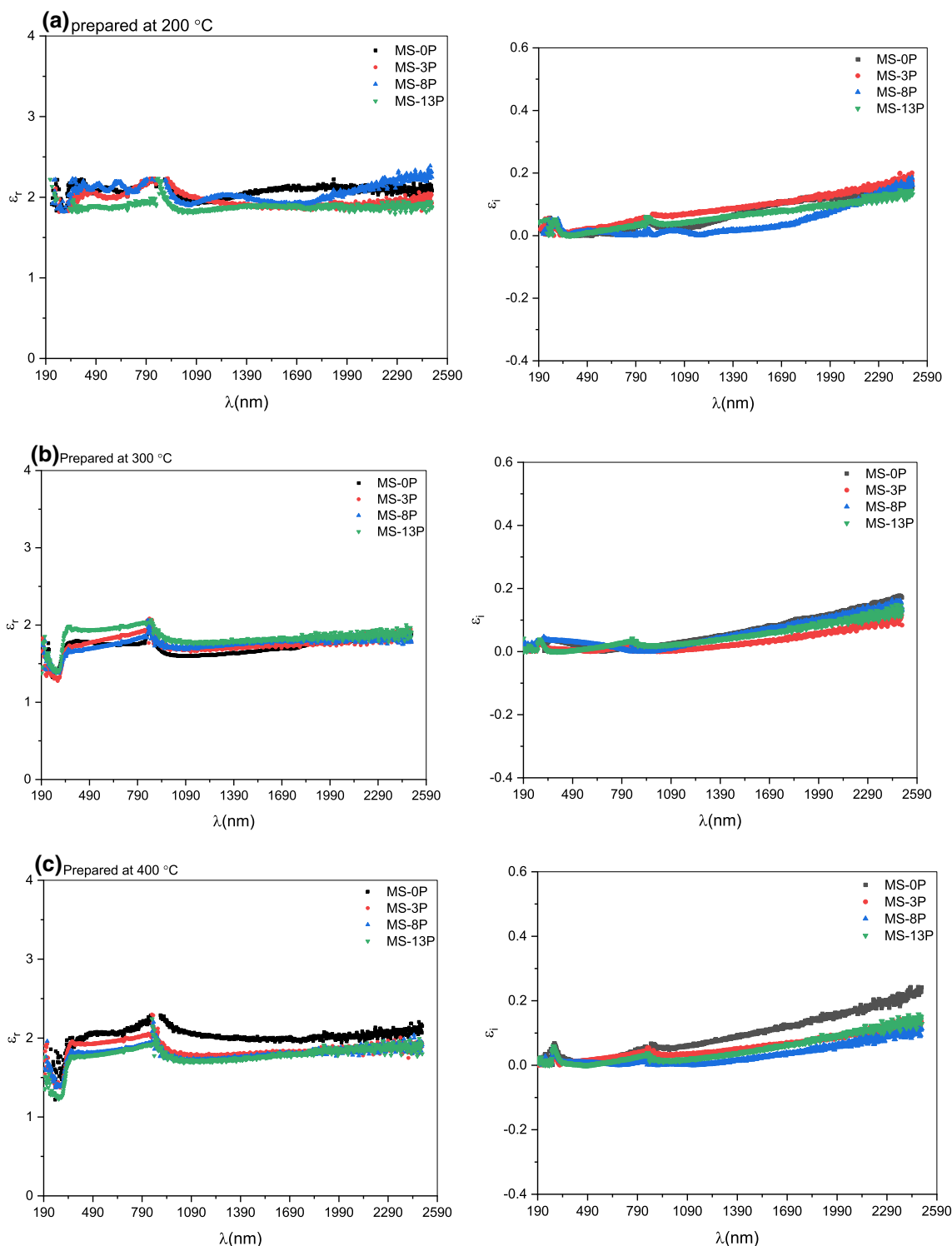


**Fig. 10** The dependence of  $\epsilon_r$  and  $\epsilon_i$  values of the fabricated films on photon wavelength at different calcination temperatures

Figure 9 shows the refractive index  $n$  of the prepared thin films with different  $P_2O_5$  concentrations and calcinated at different temperatures. It is observed that the refractive index of the thin film is nearly the same (average  $n = 1.4$ ) and is uniform in the overall visible zone.

The dielectric constant is a fundamental intrinsic material property composed of real and imaginary products. The real part is associated with the property of reducing the light velocity through the material. The dielectric compo-

**Table 1** The values of the direct bandgap  $E_g$  and the Urbach’s energy  $E_u$

Preparation temp. (°C)	P <sub>2</sub> O <sub>5</sub> content (wt%)	$E_u$ (eV)	$E_g$ (eV)
200	0	0.1731	4.022
	3	0.2375	3.997
	8	0.2329	3.982
	13	0.1922	3.971
300	0	0.2238	4.010
	3	0.3959	3.948
	8	0.4993	3.914
	13	0.2738	3.886
400	0	0.3514	3.982
	3	0.2217	3.886
	8	0.3018	3.856
	13	0.2562	3.839

nents (real ( $\epsilon_r$ ) and imaginary ( $\epsilon_i$ )) are determined using the relations [48].

$$\epsilon_r = n^2 - k^2 \tag{6}$$

$$\epsilon_i = 2nk \tag{7}$$

The dependence of  $\epsilon_r$  and  $\epsilon_i$  values of the fabricated films on photon wavelength at different calcination temperatures are shown in Fig. 10a–c, respectively. It can be observed that the behavior of the real product of dielectric is similar to that of the refractive index while the imaginary product depends on the extinction coefficient.

For  $\alpha < 10^4 \text{ cm}^{-1}$ , Urbach tail takes place where  $\alpha$  is exponentially associated with the incident light energy ( $h\nu$ ) by the next empirical formulation [4]:

$$\alpha(h\nu) = \alpha_0 e^{h\nu/E_u} \tag{8}$$

where  $\alpha_0$  represents an initial absorption coefficient which is a constant.  $E_u$  stands for the localized state’s width in the gap region that shows the amorphous material degree of disorder. From the relation among the natural logarithm of calculated absorption coefficient ( $\ln \alpha$ ) and the incident pho-

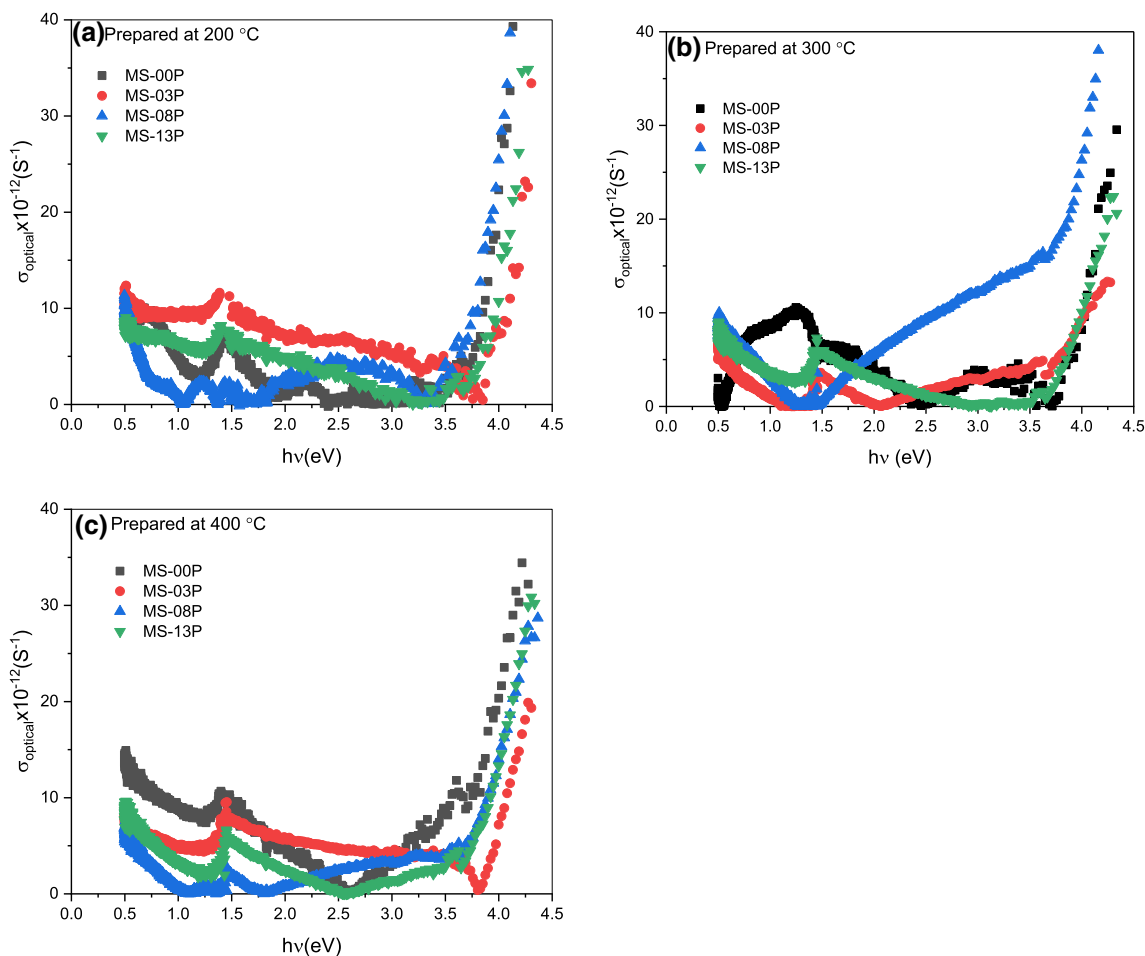


**Fig. 11** The optical conductivity of P<sub>2</sub>O<sub>5</sub> doped MgSiO<sub>3</sub> (0, 3, 8, and 13 wt%) thin films calcinated at different temperatures (200, 300, and 400 °C)

ton energy ( $h\nu$ ) for the manufactured films (not included), the slope resulted from straight lines from these relations gives the value of  $E_u$ , and the initial absorption coefficient ( $\alpha_0$ ) is obtained from the linear relation interception. The extracted values of  $E_u$  are strongly dependent on the Sn content as well as on the preparation temperature drawn in Table 1. The dependence of  $E_u$  on the  $P_2O_5$  content has resulted from an increase of structural defects as the  $P_2O_5$  content increases [50]. These structural defects generate a large number of localized states close to the band edges and so leads to an increase of Urbach energy.

In the case of free charges existence, an electric field  $E$  is generated through a material due to the propagation of the electromagnetic waves in the  $x$ -direction. This field is reported by Maxwell formula

$$\frac{d^2 E}{dx^2} = \frac{\mu}{c^2} 4\pi\sigma \frac{dE}{dt} + \frac{\mu\varepsilon}{c^2} \frac{d^2 E}{dt^2} \quad (9)$$

where  $\mu$ ,  $\varepsilon$ ,  $\sigma$ ,  $c$  are permeability, dielectric constant, conductivity, and velocity of light, respectively. Hence, the optical conductivity ( $\sigma_{\text{optical}}$ ) could be computed with the aid of the absorption coefficient,  $\alpha$ , as follows [51]:

$$\sigma_{\text{optical}} = \frac{\alpha n c}{4\pi} \quad (10)$$

The optical conductivity of P doped  $MgSiO_3$  (0, 3, 8, and 13 wt%) thin films calcinated at different temperatures (200, 300, and 400 °C) are plotted in Fig. 11.

It was seen that the optical conductivity tacks nearly relative values and similar behaviors in all samples at all temperatures of preparation where it is constant at low energies and increases at higher incident photon energies. This behavior is mainly a result of the increase of both incident photon energy and absorption coefficient which lead to an increase of charge carriers excitation [51].

## 4 Conclusions

Mesoporous magnesium silicate transparent thin films were prepared by utilizing a sol–gel/spin-coating procedure at lower thermal calcinated 200–400 °C. By governing sol–gel reactions and changing the  $P_2O_5$  contents, homogeneous and high surface area morphology were gotten. It was established from the XRD results that the crystallinity of the films changed from completely amorphous to a crystalline phase with increasing the calcination temperature. Additionally, the Introducing of  $P_2O_5$  leads to a growth of the magnesium silicate internal structure and hinders the amorphous phase. The SEM and TEM confirm the good morphology and the particle-size for the prepared mesoporous films. The particle sizes of 13 nm to 19 nm were observed. Relative values of

transmittance in the visible region were observed for all samples as a result of surface homogeneity. The FTIR indicated the molecular interaction for the formation of the nanoporous films between the magnesium silicate and phosphorus via the silanol and phosphanol groups through the intermolecular hydrogen bonding during the sol–gel results in the successful formation of nanoporous films. The optical band gap shows a blue shift with increasing of the  $P_2O_5$  content and with the calcination temperature increase. The refractive index is nearly constant and uniform in the overall visible zone for all samples. The behavior of the real product of dielectric is similar to that of the refractive index while the imaginary product depends on the extinction coefficient. The optical conductivity shows a constant behavior at low energies and then shows an increase at higher incident photon energies as a result of an increase of charge carriers' excitation.

## References

- Lim, J.W.; Schmitt, M.L.; Brow, R.K.; Yung, S.W.: Properties and structures of tin borophosphate glasses. *J. Non. Cryst. Solids* **356**, 1379–1384 (2010). <https://doi.org/10.1016/j.jnoncrysol.2010.02.019>
- Möncke, D.; Eckert, H.: Review on the structural analysis of fluoride-phosphate and fluoro-phosphate glasses. *J. Non-Cryst. Solids X* **3**, 100026 (2019). <https://doi.org/10.1016/j.nocx.2019.100026>
- El Nahrawy, A.M.; Mansour, A.M.; Abou Hammad, A.B.; Ibrahim, R.S.; Abouelnaga, A.M.; Abdel-Aziz, M.S.: Optical, functional impact and antimicrobial of chitosan/phosphosilicate/ $Al_2O_3$  nanosheets. *J. Inorg. Organomet. Polym. Mater.* **30**, 3084–3094 (2020). <https://doi.org/10.1007/s10904-020-01469-x>
- El Nahrawy, A.M.; Hemdan, B.A.; Abou Hammad, A.B.; Abia, A.L.K.; Bakr, A.M.: Microstructure and antimicrobial properties of bioactive cobalt Co-doped copper aluminosilicate nanocrystallines. *Silicon* (2019). <https://doi.org/10.1007/s12633-019-0032-6>. (in press)
- Dahshan, A.; Hammad, A.B.A.; Aly, K.A.; El Nahrawy, A.M.:  $Eu_2O_3$  role in the optical and photoluminescence properties of  $50SiO_2-7MgO-20ZnO-(23-x)La_2O_3-xEu_2O_3$  nano-crystalline thin films. *Appl. Phys. A Mater. Sci. Process.* **126**, 1–8 (2020). <https://doi.org/10.1007/s00339-019-3207-3>
- Ye, C.; Petit, L.; Koponen, J.J.; Hu, I.N.; Galvanauskas, A.: Short-term and long-term stability in ytterbium-doped high-power fiber lasers and amplifiers. *IEEE J. Sel. Top. Quantum Electron.* **20**(5), 188–199 (2014)
- Shi, Q.; Kang, J.; Qu, Y.; Liu, S.; Khater, G.A.; Li, S.; Wang, Y.; Yue, Y.: Effect of rare-earth oxides on structure and chemical resistance of calcium aluminophosphate glasses. *J. Non. Cryst. Solids.* **491**, 71–78 (2018). <https://doi.org/10.1016/j.jnoncrysol.2018.04.010>
- Cui, J.; Wen, H.; Xie, S.; Song, W.; Sun, M.; Yu, L.; Hao, Z.: Synthesis and characterization of aluminophosphate glasses with unique blue emission. *Mater. Res. Bull.* **103**, 70–76 (2018). <https://doi.org/10.1016/j.materresbull.2018.02.044>
- Wen, H.; Xie, S.; Cui, J.; Mao, S.; Luo, L.; Brik, M.G.: Optical properties of 3d transition metal ion-doped aluminophosphate glasses. *J. Lumin.* **213**, 263–272 (2019). <https://doi.org/10.1016/j.jlumin.2019.05.016>



10. Liu, W.; Guo, X.Q.; Su, G.; Cao, L.X.; Wang, Y.G.; Duan, J.R.: A new organically-templated cobalt borophosphate with a novel borophosphatic anionic partial structure. *J. Solid State Chem.* **184**, 2538–2542 (2011). <https://doi.org/10.1016/j.jssc.2011.07.032>
11. Liang, X.; Yuan, S.; Yang, Y.; Chen, G.: Optical properties of Tb<sup>3+</sup>-Sm<sup>3+</sup>-co-doped B<sub>2</sub>O<sub>3</sub>-Al<sub>2</sub>O<sub>3</sub>-SrO glasses. *Phys. Chem. Glas. - Eur. J. Glas. Sci. Technol. Part B* **51**, 226–229 (2010)
12. Ehrhart, D.: Deep-UV materials. *Adv. Opt. Technol.* **7**, 225–242 (2018). <https://doi.org/10.1515/aot-2018-0023>
13. Elabd, A.A.; Elhefnawy, O.A.; El Nahrawy, A.M.: A new organic-silica based nanocomposite prepared for spectrophotometric determination of uranyl ions. *RSC Adv.* **6**, 9563–9570 (2016). <https://doi.org/10.1039/c5ra21401g>
14. Elokr, M.M.; Metawe, F.; El-Nahrawy, A.M.; Osman, B.A.A.A.: Enhanced structural and spectroscopic properties of phosphosilicate nanostructures by doping with Al<sub>2</sub>O<sub>3</sub> ions and calcinations temperature. *Int. J. ChemTech Res.* **9**, 228–234 (2016)
15. Wang, Y.; Wang, F.; Zhou, J.; Zhu, H.; Liao, Q.; Li, L.; Zhu, Y.; Yuan, Y.; Zhang, J.: Effect of molybdenum on structural features and thermal properties of iron phosphate glasses and boron-doped iron phosphate glasses. *J. Alloys Compd.* **826**, 154225 (2020). <https://doi.org/10.1016/j.jallcom.2020.154225>
16. Issa, S.A.M.; Saddeek, Y.B.; Sayyed, M.I.; Tekin, H.O.; Kilicoglu, O.: Radiation shielding features using MCNPX code and mechanical properties of the PbO-Na<sub>2</sub>O-B<sub>2</sub>O<sub>3</sub>-CaO-Al<sub>2</sub>O<sub>3</sub>-SiO<sub>2</sub> glass systems. *Compos. Part B Eng.* **167**, 231–240 (2019). <https://doi.org/10.1016/j.compositesb.2018.12.029>
17. Wang, B.; Chang, Q.Y.; Gao, K.; Fang, H.R.; Qing, T.; Zhou, N.N.: The synthesis of magnesium silicate hydroxide with different morphologies and the comparison of their tribological properties. *Tribol. Int.* **119**, 672–679 (2018). <https://doi.org/10.1016/j.triboint.2017.11.020>
18. Shao, Z.; He, X.; Niu, Z.; Huang, T.; Cheng, X.; Zhang, Y.: Ambient pressure dried shape-controllable sodium silicate based composite silica aerogel monoliths. *Mater. Chem. Phys.* **162**, 346–353 (2015). <https://doi.org/10.1016/j.matchemphys.2015.05.077>
19. Sprynsky, M.; NiedojadŁo, J.; Buszewski, B.: Structural features of natural and acids modified chrysotile nanotubes. *J. Phys. Chem. Solids* **72**, 1015–1026 (2011). <https://doi.org/10.1016/j.jpics.2011.05.013>
20. Savii, C.; Popovici, M.; Enache, C.; Subrt, J.; Niznansky, D.; Bakardzieva, S.; Caizer, C.; Hrianca, I.: Fe<sub>2</sub>O<sub>3</sub>-SiO<sub>2</sub> composites obtained by sol-gel synthesis. In: *Solid State Ionics*, pp. 219–227. Elsevier (2002)
21. ElNahrawy, A.M.; Mansour, A.M.; ElAttar, H.A.; Sakr, E.M.M.; Soliman, A.A.; Hammad, A.B.A.: Impact of Mn-substitution on structural, optical, and magnetic properties evolution of sodium-cobalt ferrite for opto-magnetic applications. *J. Mater. Sci.: Mater. Electron.* **31**, 6224–6232 (2020). <https://doi.org/10.1007/s10854-020-03176-2>
22. Youssef, A.M.; El-Nahrawy, A.M.; Abou Hammad, A.B.: Sol-gel synthesis and characterizations of hybrid chitosan-PEG/calcium silicate nanocomposite modified with ZnO-NPs and (E102) for optical and antibacterial applications. *Int. J. Biol. Macromol.* **97**, 561–567 (2017). <https://doi.org/10.1016/j.jbiomac.2017.01.059>
23. Serra, J.; González, P.; Liste, S.; Serra, C.; Chiussi, S.; León, B.; Pérez-Amor, M.; Ylänen, H.O.; Hupa, M.: FTIR and XPS studies of bioactive silica based glasses. *J. Non. Cryst. Solids* **332**, 20–27 (2003). <https://doi.org/10.1016/j.jnoncrsol.2003.09.013>
24. Fellah, B.H.; Layrolle, P.: Sol-gel synthesis and characterization of macroporous calcium phosphate bioceramics containing micro-porosity. *Acta Biomater.* **5**, 735–742 (2009). <https://doi.org/10.1016/j.actbio.2008.09.005>
25. Glorieux, B.; Salminen, T.; Massera, J.; Lastusaari, M.; Petit, L.: Better understanding of the role of SiO<sub>2</sub>, P<sub>2</sub>O<sub>5</sub> and Al<sub>2</sub>O<sub>3</sub> on the spectroscopic properties of Yb<sup>3+</sup> doped silica sol-gel glasses. *J. Non. Cryst. Solids* **482**, 46–51 (2018). <https://doi.org/10.1016/j.jnoncrsol.2017.12.021>
26. Karabulut, M.; Metwalli, E.; Brow, R.K.: Structure and properties of lanthanum-aluminum-phosphate glasses. *J. Non-Cryst. Solids.* **283**, 211–219 (2001). [https://doi.org/10.1016/S0022-3093\(01\)00420-3](https://doi.org/10.1016/S0022-3093(01)00420-3)
27. Šulekova, M.; Váhovská, L.; Hudák, A.; Žid, L.; Zelenák, V.: A study of 5-fluorouracil desorption from mesoporous silica by RP-UHPLC. *Molecules* (2019). <https://doi.org/10.3390/molecules24071317>
28. Kumari, P.; Dwivedi, Y.: Investigation of bright red emitting Mn doped aluminum silicate nanophosphor. *Mater. Res. Bull.* **88**, 266–271 (2017). <https://doi.org/10.1016/j.materresbull.2017.01.02>
29. Egodawatte, S.; Dominguez, S.; Larsen, S.C.: Solvent effects in the development of a drug delivery system for 5-fluorouracil using magnetic mesoporous silica nanoparticles. *Microporous Mesoporous Mater.* **237**, 108–116 (2017). <https://doi.org/10.1016/j.micromeso.2016.09.024>
30. Kajthunyakarn, W.; Sakloetsakun, D.; Pongjanyakul, T.: Sodium caseinate-magnesium aluminum silicate nanocomposite films for modified-release tablets. *Mater. Sci. Eng. C* **92**, 827–839 (2018). <https://doi.org/10.1016/j.msec.2018.07.040>
31. Farag, A.A.M.; Soliman, H.S.; Atta, A.A.: Analysis of dark and photovoltaic characteristics of Au/Pyronine G(Y)/p-Si/Al heterojunction. *Synth. Met.* **161**, 2759–2764 (2012). <https://doi.org/10.1016/j.synthmet.2011.10.017>
32. El Nahrawy, A.M.; Mansour, A.M.; Abou Hammad, A.B.; Wassel, A.R.: Effect of Cu incorporation on morphology and optical band gap properties of nano-porous lithium magnesio-silicate (LMS) thin films. *Mater. Res. Express* **6**, 016404 (2019). <https://doi.org/10.1088/2053-1591/aac343>
33. Nahrawy, A.M.E.; Hammad, A.B.A.; Bakr, A.M.; Wassel, A.R.: Adjustment of morphological and dielectric properties of ZnTiO<sub>3</sub> nanocrystalline using Al<sub>2</sub>O<sub>3</sub> nanoparticles. *Appl. Phys. A Mater. Sci. Process.* (2019). <https://doi.org/10.1007/s00339-018-2350-6>
34. Mansour, A.M.; Nasr, M.; Saleh, H.A.; Mahmoud, G.M.: Physical characterization of 5',5''-dibromo-o-cresolsulphophthalen (BCP) spin-coated thin films and BCP/p-Si based diode. *Appl. Phys. A Mater. Sci. Process.* **125**, 1–11 (2019). <https://doi.org/10.1007/s00339-019-2920-2>
35. Hassan, N.; Mansour, A.M.M.; Roushdy, N.; Farag, A.A.M.A.M.; Osiris, W.G.G.: Optical sensing performance characteristics of Schottky devices diodes based nano-particle disodium 6-hydroxy-5-[(2-methoxy-5-methyl-4-sulfophenyl)azo]-2-naphthalenesulfonate thin films: a comparison study. *Optik (Stuttgart)* **158**, 1255–1265 (2018). <https://doi.org/10.1016/j.ijleo.2017.12.203>
36. Hemdan, B.A.; El Nahrawy, A.M.; Mansour, A.M.; Hammad, A.B.A.: Green sol-gel synthesis of novel nanoporous copper aluminosilicate for the eradication of pathogenic microbes in drinking water and wastewater treatment. *Environ. Sci. Pollut. Res.* **26**, 9508–9523 (2019). <https://doi.org/10.1007/s11356-019-04431-8>
37. Farag, A.A.M.A.M.M.; Mansour, A.M.M.; Ammar, A.H.H.; Rafea, M.A.A.: Characterization of electrical and optical absorption of organic based methyl orange for photovoltaic application. *Synth. Met.* **161**, 2135–2143 (2011). <https://doi.org/10.1016/j.synthmet.2011.08.015>
38. Mansour, A.M.; El Radaf, I.M.: Structural, optical and electrical properties of CuBiS<sub>2</sub> thin films deposited by spray pyrolysis at different deposition times. *Int. J. Microstruct. Mater. Prop.* **14**, 419 (2019). <https://doi.org/10.1504/ijmmp.2019.102219>
39. El Nahrawy, A.M.; Abou Hammad, A.B.; Abdel-Aziz, M.S.; Wassel, A.R.: Spectroscopic and antimicrobial activity of hybrid chitosan/silica membranes doped with Al<sub>2</sub>O<sub>3</sub> nanoparticles. Sili-



- con **11**, 1677–1685 (2019). <https://doi.org/10.1007/s12633-018-9986-x>
40. El Nahrawy, A.M.; Hammad, A.B.A.; Youssef, A.M.; Mansour, A.M.; Othman, A.M.: Thermal, dielectric and antimicrobial properties of polystyrene-assisted/ITO: Cu nanocomposites. *Appl. Phys. A Mater. Sci. Process.* **125**, 46 (2019). <https://doi.org/10.1007/s00339-018-2351-5>
41. Kanyathare, B.; Asamoah, B.O.; Ishaq, U.; Amoani, J.; Rätty, J.; Peiponen, K.E.: Optical transmission spectra study in visible and near-infrared spectral range for identification of rough transparent plastics in aquatic environments. *Chemosphere* **248**, 126071 (2020). <https://doi.org/10.1016/j.chemosphere.2020.126071>
42. Niskanen, I.; Peiponen, K.E.; Rätty, J.: Assessment of refractive index of pigments by gaussian fitting of light backscattering data in context of the liquid immersion method. *Appl. Spectrosc.* **64**, 558–561 (2010). <https://doi.org/10.1366/000370210791211754>
43. Çayır Taşdemirci, T.: Influence of annealing on properties of SILAR deposited nickel oxide films. *Vacuum* **167**, 189–194 (2019). <https://doi.org/10.1016/j.vacuum.2019.05.047>
44. El Nahrawy, A.M.; Montaser, A.S.; Abou Hammad, A.B.; Ezzat, M.; El-Shakankery, M.: Copper lithium silicate/ZrO<sub>2</sub> nanoparticles-coated Kevlar for improving UV-Vis absorbance/protection properties. *Silicon* (2019). <https://doi.org/10.1007/s12633-019-00271-w>
45. Liu, L.; Qin, N.; Bao, D.: Structural, optical, and photoluminescent properties of sol-gel derived Eu-doped Ba<sub>1-x</sub>Sr<sub>x</sub>TiO<sub>3</sub> thin films. *J. Mater. Sci.: Mater. Electron.* **26**, 3403–3408 (2015). <https://doi.org/10.1007/s10854-015-2847-0>
46. Omar, N.A.S.; Fen, Y.W.; Matori, K.A.; Zaid, M.H.M.; Norhafizah, M.R.; Nurzilla, M.; Zamratul, M.I.M.: Synthesis and optical properties of europium doped zinc silicate prepared using low cost solid state reaction method. *J. Mater. Sci.: Mater. Electron.* **27**, 1092–1099 (2016). <https://doi.org/10.1007/s10854-015-3856-8>
47. El Nahrawy, A.M.; Ali, A.I.; Abou Hammad, A.B.; Mbarek, A.: Structural and optical properties of wet-chemistry Cu co-doped ZnTiO<sub>3</sub> thin films deposited by spin coating method. *Egypt. J. Chem.* **61**, 1073–1081 (2018). <https://doi.org/10.21608/ejchem.2018.4069.1359>
48. Nahrawy, A.M.El: Structural studies of sol gel prepared nanocrystalline silica zinc titanate ceramic. *Int. J. Adv. Eng. Technol. Comput. Sci.* **2**, 15–18 (2015)
49. Mansour, A.M.: Fabrication and characterization of a photodiode based on 5',5''-dibromo-*o*-cresolsulphophthalein (BCP). *Silicon* **11**, 1–8 (2018). <https://doi.org/10.1007/s12633-018-0016-9>
50. Darwish, A.A.A.; Rashad, M.; Bekheet, A.E.; El-Nahass, M.M.: Linear and nonlinear optical properties of GeSe<sub>2-x</sub>Sn<sub>x</sub> (0 ≤ x ≤ 0.8) thin films for optoelectronic applications. *J. Alloys Compd.* **709**, 640–645 (2017). <https://doi.org/10.1016/j.jallcom.2016.08.280>
51. El-Diasty, F.; Aly, E.H.; El-Sawy, N.M.: Optical and two-photon absorption analysis of radiation-grafted fluoropolymer. *J. Polym. Sci. Part B Polym. Phys.* **48**, 2045–2051 (2010). <https://doi.org/10.1002/polb.22084>

